Impact of Global Warming on U.S. Summertime Mesoscale Convective Systems: A Simple Lagrangian Parcel Model Perspective

Qiu Yang,[a] L. Ruby Leung,[a] Zhe Feng,[a] Xingchao Chen[b]

[a] *Atmospheric Sciences and Global Change Division, Pacific Northwest National Laboratory, Richland, Washington, USA*

[b] *Department of Meteorology and Atmospheric Science, and Center for Advanced Data Assimilation and Predictability Techniques, The Pennsylvania State University, PA, USA*

Corresponding author: Qiu Yang, qiu.yang@pnnl.gov

ABSTRACT: Mesoscale convective systems (MCSs) are the dominant rainfall producer over the U.S. during the warm season, causing natural disasters and severe weather every year. Global climate models have large uncertainty in projecting precipitation changes in the future climate. Here a simple Lagrangian parcel model is used to investigate the impact of global warming on MCS initiation and growth. The single-column parcel model projects a mean precipitation decrease over the central U.S. and an increase to its east, in agreement with the CMIP5 model projection. It also highlights the crucial role of current climate mean state model bias in exaggerating the change in future mean precipitation projection by 25%. As for convective population, the model captures the decreased occurrence frequency of weak to moderate convection and increased frequency of strong convection due to the increased CAPE and CIN, in agreement with convection-permitting regional simulations. Novel parameterizations of gust front propagation speed and subsidence strength are developed as guided by cloud-resolving simulations. The multi-column parcel model employing those parameterizations captures readily the cold pool-induced upscale growth feature. It simulates smaller mesoscale clusters over the central U.S. under global warming due to gust front slowdown and subsidence strength enhancement, which is further attributed to land aridity-induced weakening of initial accumulated precipitation and strengthening of updraft speed, respectively. That said, mesoscale clusters could become bigger under more favorable conditions in future climate, including boundary layer moistening, convection life time lengthening, and cold pool mechanical lifting enhancement, which require further investigations to improve mechanistic understanding of future MCS changes.

1. Introduction

A mesoscale convective system (MCS) is a complex of thunderstorms that is typically organized over hundreds of kilometers and persists for several hours or more (**??**). MCSs are ubiquitous in tropics, subtropics, and midlatitudes, having a significant impact on local weather and hydrologic cycle through massive release of rainfall (**????????**). In particular, long-lived and intense MCSs are frequently initiated to the east of the Rocky Mountains and propagate eastward afterwards, accounting for more than 50% of warm season precipitation in the Great Plains (**?**). Due to its higher intensity and larger area coverage than non-MCS, MCS rainfall produces more surface runoff than non-MCS rainfall (**?**) and contributes to the majority of slow-rising and hybrid floods during the warm season in the U.S. (**?**). Besides, the dynamics of MCSs in the central U.S. show significant interactions with eastward propagating large-scale environments (**??**) as well as soil moisture (**?**). The crucial role of MCSs in influencing atmospheric conditions over the U.S. provides a key benchmark for testing the skills of the present-day numerical models for weather forecast and climate change projection. It is hypothesized that the long-standing warm and dry bias in the summertime central U.S. is related to the failure of coarse-resolution general circulation models (GCMs) in simulating MCSs and the associated precipitation (**??????**). In contrast, recent studies based on the multiscale modeling framework (**??**) and convection-permitting regional simulations (**??**) show some encouraging progress in capturing realistic features of MCSs and the associated precipitation. That said, a better understanding of the underlying mechanisms throughout the whole MCS life cycle is still lacking.

The crucial role of MCSs in the water cycle underscores the necessity of investigating its future changes under global warming. Thanks to the improved modeling and computing capabilities, convection-permitting regional simulations have now become a useful and practical tool to investigate the behaviors of MCSs and precipitation response in future climate. For example, **?** undertook two 13-year high-resolution climate change simulations at convection-permitting resolution, one of which is driven by initial and boundary conditions from current climate and the other is forced with warmer and moister perturbed boundary conditions in the pseudo-global warming (PGW) framework. The present-day convection permitting regional simulation was validated against observational datasets and the PGW experiments were proved to be useful for demonstrating a new mechanism for warm-season precipitation response to global warming (**?**), investigating the future

intensification of hourly precipitation extremes (**?**), and simulating the convective precipitation diurnal cycle in both current and future climate (**?**). In particular, **?** showed that weak to moderate convection will decrease and strong convection will increase in frequency in a future climate, which was further attributed to the increasing convective available potential energy (CAPE) and convective inhibition (CIN) downstream of the Rockies in a future climate. **?** further concluded that intense summertime MCS frequency will more than triple in North America and the combined effect of increasing maximum precipitation rates and heavy precipitation area contributes to 80% increases in the total MCS precipitation volume. These studies indicate the significant impact of global warming on both convective initiation and MCS genesis, the two early stages of MCS life cycle. However, due to the heavy computational expense, using convection-permitting regional simulations is not an affordable way to discuss the impact of global warming on MCS initiation and growth under various favorable/unfavorable conditions and complex mesoscale forcing, let alone isolating key mechanisms response for its behavior change in future climate. Furthermore, even convection permitting modeling faces challenges in realistically simulating summertime MCSs in the central U.S. (**?**), motivating the need to further investigate how summertime MCSs may change with global warming.

To theoretically understand how summertime MCS would change under global warming, it is important to isolate the key mechanisms of change related to convective initiation and MCS genesis, respectively. Previous studies used single-column models to discuss thermodynamic and dynamic constraints for convective initiation (**????**). The upscale growth feature during MCS genesis resembles the convective self-aggregation phenomenon that scattered small-scale convection is aggregated to several isolated mesoscale clusters in radiative-convective equilibrium simulations. The underlying mechanisms for convective self-aggregation are attributed to the interactions between clouds, moisture, radiation, surface fluxes, and circulation (**??????**), boundary layer diabatic processes (**?**), and convection-gravity wave interactions (**???**). In particular, it has been shown that cold pools resulting from downdrafts and rain evaporation help trigger new convection in the vicinity of existing convective storms, leading to convective organization (**??**). Novel tracking algorithms were designed to track cold pool gust fronts, confirming that cold pools can influence the initiation of new convective cells (**???**). High-resolution cloud-resolving simulations further highlight the stronger convection triggering effects by cold pool collision than

that by isolated cold pools (**???**). **?** conceptualized cold pool interactions into a parameter-free mathematical model and successfully developed a simple model for convective self-aggregation (**?**). That said, a simple unified framework for modeling both convective initiation and MCS genesis and isolating their corresponding bare-bone mechanisms is still lacking.

Recently, **?** developed a simple Lagrangian parcel model for capturing the basic features of summertime convective initiation over the central U.S. and understanding the salient mechanisms necessary for reproducing the upscale growth feature during MCS genesis. To achieve that, a simple single-column Lagrangian parcel model is first developed by considering conservation laws of mass, momentum, and energy, condensation and precipitation, as well as entrainment process for a rising parcel. This single-column model was useful for investigating the collective effects of boundary layer moistening and dynamical lifting on convective initiation, studying the diurnal cycle of convective initiation and identifying the differences between cases with/without MCS initiation, and exploring the impact of global warming on convective initiation and theoretically predicting the convection population under climate change. Then this single-column model was further extended to a multi-column model that includes an array of single-column models aligned in the east–west direction and incorporates idealized cold pool interaction mechanisms. The multi-column model captures readily the cold pool–induced upscale growth feature during MCS genesis from initially scattered convection in a few hours. It also highlights the crucial role of lifting effects due to cold pool collision and spreading, subsidence effect, and gust front propagation speed in controlling the final size of mesoscale clusters and cold pool regions. Nevertheless, all these controlling factors were fixed as some constant value for simplicity but should vary in a more realistic way when assessing the impact of global warming.

The overall goal of this study is to investigate the impact of global warming on the convective initiation and genesis of summertime MCSs over the U.S. based on this simple Lagrangian parcel model and highlight the key underlying mechanisms responsible for the MCS behavior changes during the convective initiation and MCS genesis stages of MCS life cycle.

All our discussion in this study is based on the simple Lagrangian parcel model (**?**), including a single-column model for convective initiation and a multi-column model for MCS genesis, but additionally with some modifications. Specifically, the single-column model is modified by using a better parameterization of entrainment process, while the multi-column model is further

improved by incorporating realistic parameterizations of gust front propagation speed and subsidence strength guided by cloud-resolving simulations. After specifying environmental profiles and initial conditions, the parcel behavior in the single-column model is used to assess the favorability for convective initiation, while the collective behavior of parcels in the multi-column model is interpreted as the upscale growth feature during MCS genesis. To examine the impact of global warming, we choose to use the PGW approach (**???**) where the future climate is approximated by the current climate plus a climate perturbation derived from GCM ensemble projection of mean climate change. To assess the impact of global warming on convective initiation, we run the single-column model multiple times for each 1deg-by-1deg grid over the U.S. driven by all hourly environmental profiles during a 14-year summertime period, and investigate the global warming driven changes in terms of climatological mean precipitation, its sensitivity to current climate mean state model bias, and convective population. To assess the impact of global warming on MCS genesis, we run the multi-column model with the large-scale environmental profile averaged over the central U.S. and investigate the global warming driven changes in mesoscale cluster size, cold pool area, and convective cell number.

The results highlight the key mechanisms responsible for the MCS behavior changes during the convective initiation and MCS genesis stages in the future climate. By using the single-column model, we first investigate the future climatological mean precipitation changes under global warming and compare with the CMIP5 model projection. Then we discuss the changes in convective population as well as their dependence on geographic location. The simple model provides an analog testbed to illustrate the impact of biases in current climate in predicting future mean precipitation in the GCM. The multi-column model is then used to discuss the potential changes of MCS final state caused by land aridity, boundary layer moistening, convection lifetime lengthening and cold pool mechanical lifting enhancement under global warming.

The rest of the paper is organized as follows. Section 2 summarizes the single- and multi-column models and particularly the modifications, input datasets, and experimental setup. Section 3 uses the single-column model to assess the impact of global warming on convective initiation in terms of climatological mean precipitation, their sensitivity to current climate mean state model bias, and convective population. Section 4 uses the multi-column model to assess the impact of global warming on MCS genesis, emphasizing the dependence of MCS genesis on gust front propagation

speed and subsidence strength, and illustrating the changes in MCS genesis due to land aridity and other favorable conditions under global warming. The paper concludes with a discussion in section 5.

2. Methodology

In this section, we first briefly summarize the derivation details and basic properties of the single-column and multi-column Lagrangian parcel models, which was developed by **?** to understand the initiation of summertime MCSs over the central U.S. Then we describe the parameterization development for gust front propagation speed and subsidence strength under the guidance of two sets of cloud-resolving simulations. Lastly, we document all the information about input data for current and future environmental profiles as well as experiment setup details.

a. Single-column Lagrangian parcel model

The single-column Lagrangian parcel model describes the ascent trajectory of a buoyancy-driven parcel from the surface to the upper troposphere, mimicking the initiation of small-scale individual convection cells during the early stage of MCS initiation (**?**). The model considers several key physical processes during the ascent motion of the parcel, including the imbalance between buoyancy, gravity, and momentum drag, the phase change between water vapor and liquid water, and the environmental mass exchange through entrainment. The readers are referred to **?** for detailed governing equations (Table 1 of **?**), key parameters and microphysical closure (Table 2 of **?**), and explanations (Section 2a of **?**).

Compared with **?**, we further improve the parameterization of entrainment process by allowing its dependence on updraft speed (see ϵ in Table 1). Specifically, besides its dependence on parcel volume, the strength of entrainment rate ϵ is modified to be linearly proportional to the updraft speed w^+ so that entrainment process is significant only if the updraft speed of the parcel is strong and positive (**?**). Without this modification, the entrainment rate of the parcel is always significant, even in the initial and final stages when the updraft speed is low. Consequently, a parcel that is initialized with a less favorable condition for convection can still rise to upper levels due to the entrainment of environmental moisture and ends up with a large mass in the equilibrium state. Such

an unrealistic scenario was not considered in **?** where parcels are typically initialized with favorable conditions for convection, but becomes possible in this study with general initial conditions.

TABLE 1. Cloud microphysical closure and parameterizations of gust front speed and subsidence strength in the simple Lagrangian parcel model. Only modified or new parameters are listed here where the parenthesis indicates the original value or expressions in **?**. The remaining parameters in the model are the same as **?**. The notation w^+ means $w^+ = w$ if $w \geq 0$ and 0 otherwise.

Category	Symbol	Value	Description
Cloud microphysical closure	ϵ	$\epsilon = \frac{1}{\tau_{en}} \rho \left(\frac{V^*}{V}\right)^{1/3} \frac{w^+}{w^*}$	mass entrainment rate
		$(\epsilon = \frac{1}{\tau_{en}} \rho \left(\frac{V^*}{V}\right)^{1/3})$	
	w^*	$10\ m/s$	reference updraft speed
Parameterization of gust front speed	s_{gf}	$5\ m/s$ or parameterized ($5\ m/s$)	propagation speed of gust fronts
	α	$10^{-5}\ m/s/kg$	ratio coefficient between gust front speed and accumulated surface precipitation
	β	$2.0 \times 10^{-3}\ m/s^2$	decaying rate of gust front speed in time
	U_0	$4.5\ m/s$	baseline gust front speed
	δU	$5.0\ m/s$	gust front boost speed
	T_1, T_2, T_3	$2.5, 5.0, 10.0\ min$	predefined timing since the onset of surface precipitation
	ξ	0.2	fraction of surface precipitation loss due to rain evaporation
	V_d	$10\ m/s$	raindrop falling speed
Parameterization of subsidence strength	σ	3.5	ratio coefficient of subsidence below 2 km and that at 11 km
	w^*_{up}	$1.9\ m/s$ or parameterized ($1.9\ m/s$)	averaged updraft speed

In each run, a parcel is first initiated at the surface with its initial water vapor mass fraction larger than that of the environmental air by δq_v and its initial temperature the same as the environment. For the sake of simplicity, we choose not to discuss the scenarios with initial temperature perturbations, although such scenarios also happen in reality. Then the parcel gets lifted adiabatically by a certain distance, δz. After that, the parcel is released freely in the troposphere and its dynamics is completely governed by the model and model parameter values. Here the two parameters δz and δq_v represent the dynamical lifting and boundary layer moistening effects respectively, both of which should have a significant impact on the parcel dynamics. Besides, background environmental profiles including temperature and moisture are prescribed for current and future climate, serving as a controlling factor in determining the behavior of the parcel.

b. Multi-column Lagrangian parcel model

1) Model description

The multi-column Lagrangian parcel model is based on the previous single-column one and derived for modeling the collective behaviors of multiple parcels, particularly the upscale growth feature during the MCS genesis (**?**). The multi-column model considers 1000 single-column Lagrangian parcel models that are aligned in the east-west direction. The multi-column model is further augmented by incorporating the cold pool driven interaction mechanisms, including i) the lifting effect by gust front spreading, ii) the lifting effect by cold pool collision, and iii) the clear-sky subsidence effect produced by active convection. The readers are referred to **?** for more details of the model setup.

? concluded that both gust front propagation speed and subsidence strength are the controlling factors for determining the final state of the mesoscale clusters. In the following subsections 2) and 3), we develop more realistic parameterizations for both factors under the guidance of cloud-resolving simulations discussed next.

2) Cloud-resolving simulations for guiding parameterization development

Cloud-resolving simulations are useful tools for investigating convection organization and cold pool dynamics (**??**). Two sets of 2-D nonrotating cloud-resolving simulations based on the System for Atmospheric Modeling (SAM) (**?**), version 6.11.1, are used here as a guidance for parameterizing gust front propagation speed and subsidence strength. In general, the SAM has been used widely to simulate convection in idealized domain geometry (**????**). All simulations use the Smolarkiewicz's MPDATA advection scheme with monotonic corrector, the 1.5-order closure (prognostic SGS turbulent kinetic energy) subgrid-scale scheme, the CAM3 radiation package as well as the single-moment microphysics scheme (**?**). The surface of the domain is set as land with intermediate soil wetness (0.5) and typical roughness length (0.1) for the central U.S. Both interactive surface flux and radiation (shortwave and longwave) schemes are switched on to allow convection-moisture-surface flux-radiation interaction, which is crucial for convective self-aggregation phenomenon (**?**). The domain has periodic boundary conditions in zonal direction and a 27-km vertical extent. The initial background sounding is set at the state of rest and zonal winds are nudged towards zero

with a time scale of 1 day. A sponge layer is added in the upper one-third of the model domain to damp gravity waves.

The first set of 25 SAM simulations is for parameterizing gust front propagation speed. To generate a cold pool from an individual convection cell, we initiate a warm bubble in the middle of the domain at height 0.5 km with 4-km horizontal radius and 1-km vertical radius (part of the warm bubble is below the surface). The initial temperature perturbation of the warm bubble is fixed at 5 K, while its initial water vapor perturbation is varied every 0.5 g/kg from 7 g/kg to 9 g/kg. The initial temperature and moisture sounding is representative of 14-year (2004-2017) climatological mean summertime environments over the central U.S. from ERA5. To test the sensitivity of cold pools to the environment, we further vary the background moisture sounding by multiplying a constant (0.9, 0.95, 1.0, 1.05, 1.1). This 2-D mesoscale domain has 102.4-km zonal extent in a 100-m horizontal grid spacing. All simulations are run for 2 hours with a 3-sec time step. To better resolve the cold pool dynamics in the lower troposphere, these simulations use a vertical grid with 30-m grid spacing below 1 km, 60-m grid spacing between 1 km and 2 km, 100-m grid spacing between 2 km and 5 km.

The second set of 11 SAM simulations is for parameterizing subsidence strength. To promote convective self-aggregation, we initiate some white noise in the temperature field near the surface to trigger convection and run the model till it reaches the radiative-convective equilibrium (RCE) state. The initial temperature and moisture sounding is representative of climatological mean summertime environments over the central U.S. To test the sensitivity of self-aggregation to the environment, we further vary the background moisture sounding by multiplying a constant (0.5, 0.6,0.7...1.5). This 2-D synoptic domain has 1024-km zonal extent in a 2-km horizontal grid spacing. All simulations are run for 50 days with a 5-sec time step. It turns out that these simulations typically reach the RCE state in 15 days.

3) Parameterization development and sensitivity

It is worth noting that both gust front propagation speed s_{gf} and the averaged updraft speed w^*_{up} in subsidence strength are set as constant ($s_{gf} = 5\ m/s$, $w^*_{up} = 1.9\ m/s$) in the multi-column model of **?** . Such a simplification assumption may not be realistic, considering the facts that the gust front propagation speed typically slows down as the cold pool expands and the subsidence strength

should be related to the updraft speed over the neighboring convective regions (**??**). For gust front propagation speed, we run a set of 25 SAM warm bubble simulations where the background moisture profile and warm bubble initial moisture anomaly are perturbed about the reference value in the control run ($1.0 \times Q_v$ background moisture profile and 8 g/kg initial moisture anomaly). Then we diagnostically calculate the surface precipitation rate and gust front propagation speed in each simulation, which is used as a guidance for developing a new parameterization. Similar steps are taken to develop the parameterization of subsidence strength, based on a set of 11 SAM simulations in the RCE state. Details about these two sets of SAM simulations can be found in Sec. 2c.

Fig. 1a shows a snapshot of temperature anomalies from the background sounding in the control run at 40 $mins$. In general, the initial warm bubble rises gradually towards the upper levels since initiation and releases large amounts of rainfall after reaching saturation. Due to rain evaporation, the resulting cold and dense air in the downdraft hits the surface and forms the cold pool that expands in both directions. The updraft motion in the gust front indicates its lifting effects, potentially triggering new convection in the neighboring regions (**?**). The mean surface precipitation over the whole domain in panel (b) starts to increase at 18 $mins$, reaches its peak at 25 $mins$, and then decay gradually afterwards, following the dissipation of the warm bubble initiated convection. The gust front propagation speed in individual simulations shows large differences, which is generally faster in wet cases (red curves) and slower in dry cases (blue curves). Such a positive relationship between background moisture profile and gust front propagation speed is quite apparent in the first 25 $mins$ (Fig. 1c). After 25 $mins$, the surface precipitation exhibits an oscillatory pattern with a few peaks, due to the fluctuation of gust front speeds as they move to the neighboring area while affected by turbulent mixing. As for the mean gust front propagation speed in panel (c), it is initialized at time 20 $mins$, a few minutes later than the surface precipitation in panel (b), while it reaches its peak at time 23 $mins$, a few minutes earlier than surface precipitation. After 23 $mins$, the propagation speed decays dramatically in the first 5 $mins$ and then slows down gradually afterwards. When compared with the mean speed, the gust front propagation speed in individual simulations exhibits much larger value in its peak and more oscillatory patterns in the decaying stage. Such oscillatory gust front propagation speed can be induced by a few factors, such as the unsteady downdraft mass flux and the complex interactions among cold pools, surface fluxes,

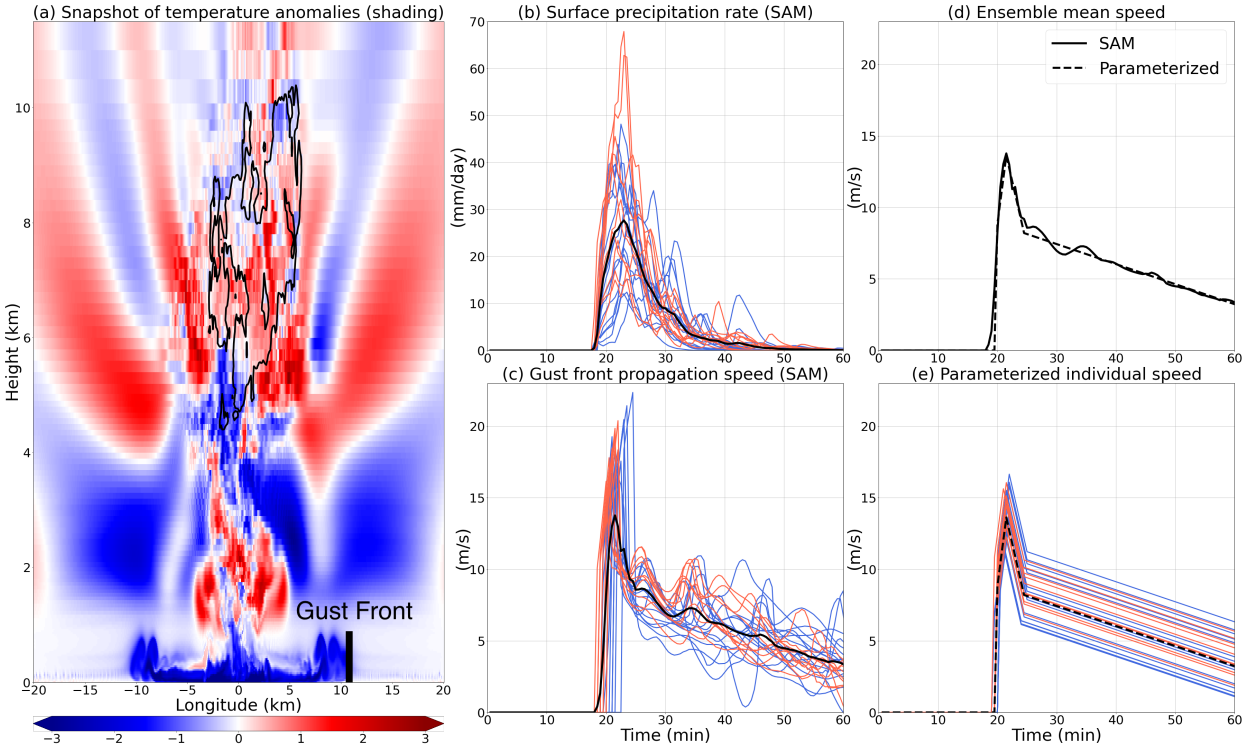

FIG. 1. Parameterization of gust front propagation speed based on 25 SAM warm bubble simulations. Panel (a) shows a snapshot of the SAM simulation with $1.0\times Q_v$ background moisture profile and 8 g/kg warm bubble moisture perturbation at 40 mins. The color shading shows temperature anomalies from background sounding and the single contour is for non-precipitating condensate (water+ice) at 0.2 g/kg. The black vertical line near the surface indicates the location of the eastward-moving gust front determined by the algorithm. Panel (b) shows the time series of surface precipitation rate from 25 SAM simulations with different moisture background profiles and warm bubble moisture perturbations (blue curves for drier cases and red curves for more moist cases). The bold black curve shows their mean. Panel (c) is similar to panel (b) but for gust front propagation speed determined by the algorithm. Panel (d) shows the time series of gust front propagation speed from (solid) SAM simulation ensemble mean, (dashed) parameterization. Panel (e) is similar to panel (d) but for individual SAM simulations.

and convection-induced turbulent flows. The reason is because different simulations have different initiation timing of gust front propagation. Moreover, the dry cases (blue curves) have much later initiation timing, faster peak speed and slower mean speed in the decaying stage. Dry cases take longer time to form the cold pool near the surface. Meanwhile, the first wave of downdraft cold

air induces more abrupt acceleration effects to the cold pool edge and fast peak propagation speed. Due to the small surface precipitation, downdraft that serves as driving force can not be maintained as the cold pool expands, resulting in slower mean gust front propagation speed.

As guided by the cloud-resolving simulations in panels (b) and (c), the gust front propagation speed consists of two parts, one of which is for the short-time speed boost in the first few minutes after cold pool initiation and the other is the linearly decaying trend throughout the whole duration. Thus the detailed parameterization is formulated as follows,

$$s = s_1 + s_2, \tag{1}$$

$$s_1 = \begin{cases} 0 & \text{if } t < T_1 \\ \frac{t-T_1}{T_2-T_1}\delta U & \text{if } T_1 \le t < T_2 \\ \frac{T_3-t}{T_3-T_2}\delta U & \text{if } T_2 \le t < T_3 \\ 0 & \text{if } t \ge T_3 \end{cases} \tag{2}$$

$$s_2 = \begin{cases} 0 & \text{if } t < T_1 \\ \alpha P(T_1) + U_0 - \beta(t-T_1) & \text{if } t \ge T_1 \end{cases} \tag{3}$$

where $P(t)$ represents the accumulated surface precipitation, $\alpha, \beta, U_0, \delta U$ are tunable parameters and coefficients whose value is determined through the fitting method. T_1, T_2, T_3 are the predefined timing for the gust front initiation, the peak of gust front propagation speed, and the end of the first decaying stage, respectively. Fig. 1d shows the close match between the parameterization and the mean propagation speed from panel (c), reflecting the skill of the parameterization in capturing the complex evolution of cold pool expansion dynamics. Furthermore, the parameterization also captures readily the spread of gust front propagation speed in all cases in panel (e), where the majority of wet cases have a faster speed above the mean and that of dry cases is slower.

As for the subsidence, we first diagnostically calculate its strength in the 11 SAM RCE simulations and use the results as guidance for developing the parameterization. To filter out high-frequency gravity wave signals, the vertical velocity field is first filtered by taking daily mean and spatial smoothing over a 20-km moving window. Fig. 2a shows the last-day mean of vertical velocity from the reference SAM RCE simulation ($1.0 \times Q_v$ environmental moisture profile), which features a single convective cluster to the left side of the domain and compensating subsidence prevailing in

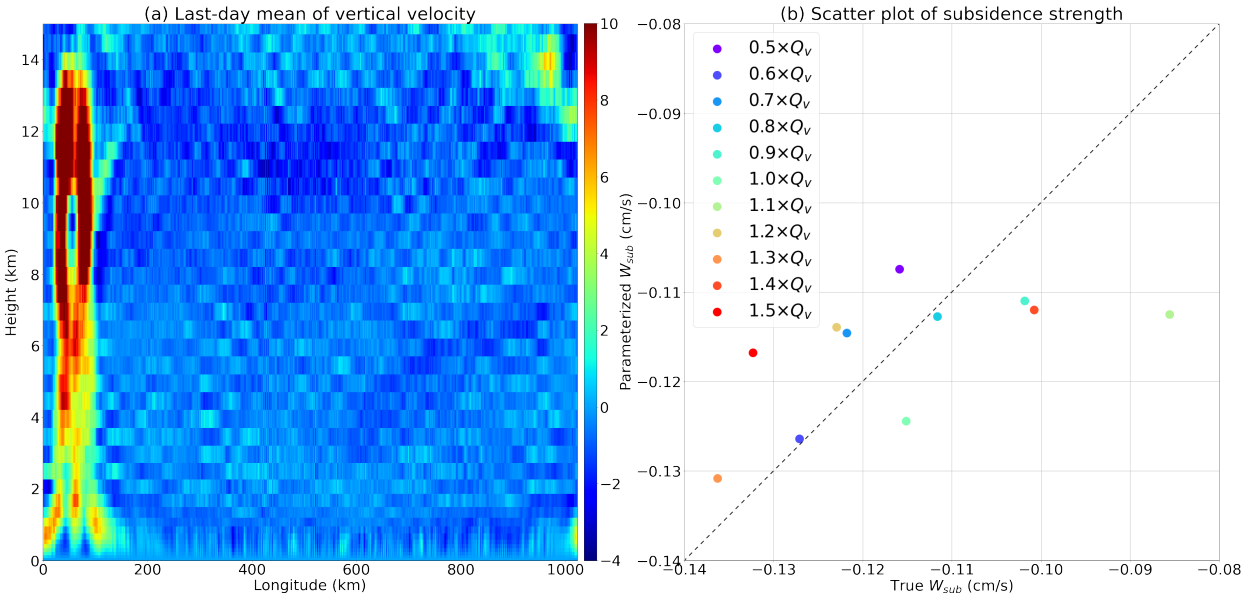

FIG. 2. Parameterization of subsidence strength based on 11 SAM RCE simulations. Panel (a) shows the last-day mean vertical velocity (unit: cm/s) from the SAM simulation with $1.0\times Q_v$ background moisture profile. The vertical velocity is further smoothed zonally by using the 1-D uniform filter over a 20-km window. Panel (b) shows the scatter plot of subsidence strength between SAM simulations and the parameterization. The overlaid dashed line is the 1:1 line. Dots in different colors correspond to the SAM simulations with different background moisture profiles as shown in the legend. For each dot, its x- and y-axis values are based on the last 20-day average of daily mean simulation output.

the remaining area. The updraft motion reaches the upper troposphere with its maximum near 11 km. The subsidence strength in these cloud-resolving simulations is then calculated by averaging of vertical velocity at lower levels below 2 km over the suppressed convection regions, which are defined as columns with no updraft speed at height 11 km. It is worth noting that 2 km is the cloud base level in the simple model.

The parameterization of subsidence strength is based on the conservation law of mass so that updraft and downdraft mass flux should be balanced at all vertical levels within the model domain. Specifically, we have $N_{conv}\bar{w}_{up} + N_{sup}w_{sub} = 0$ at the level 11 km, where $\bar{w}_{up} = \frac{1}{N_{conv}} \sum_{active} w_{up}$ is the mean updraft speed averaged over N_{conv} active convection columns and subsidence is assumed to be uniform over N_{sup} suppressed columns. Furthermore, if we assume the relative strength of subsidence at the lowest 2 km and 11 km is σ, we can obtain the parameterization of subsidence

strength at the lowest 2 km as follows,

$$w_{para} \approx \sigma w_{sup} = -\sigma \bar{w}_{up} \frac{N_{conv}}{N_{tot} - N_{conv}}, \tag{4}$$

where N_{tot} and N_{conv} denote the number of total and active convection columns, respectively, satisfying the constraint $N_{conv} + N_{sup} = N_{tot}$. Fig. 2b shows the scatter plots of parameterized and simulated subsidence strength in all 11 SAM RCE simulations with most dots located near the $y = x$ line, reflecting the skill of the simple parameterization in capturing the subsidence strength in cloud-resolving simulations in the presence of complex physical processes. The coefficient value σ is chosen accordingly through the fitting method. Surprisingly, the green outlier ($1.1 \times Q_v$) corresponds to a case with dryness close to the default one ($1.0 \times Q_v$), which may be worth further investigation.

Before implementing the parameterization of gust front propagation speed in Eqs. 1-2 and subsidence strength in Eq. 4, we need to take extra steps to obtain surface precipitation and updraft speed that are used in the parameterizations based on the multi-column model output. First, the multi-column model currently does not include the surface precipitation, but only the instantaneous precipitation rate at the height z_p of the parcel. Here we diagnostically calculate the accumulated surface precipitation by assuming a constant speed of falling raindrops, $V_d = 10\ m/s$ (**?**) and fixed fraction of rain evaporation $\xi = 0.2$ (**?**) so that only $1 - \xi$ of precipitation amount from the parcel will reach the surface at a time lag $\frac{z_p}{V_d}$. Besides, the updraft speed over convective columns at height 11 km is not available in the model as it only resolves the updraft speed of the parcel at a specific level at each time step. Here we drop the constraint of 11 km and take the average of all parcel updraft speed over convective columns to approximate the mean updraft speed. Thus Eq. 4 reads as follows,

$$w_{para} = -\sigma w^*_{up} \frac{N_{conv}}{N_{tot} - N_{conv}}. \tag{5}$$

where $w^*_{up} = \frac{1}{N_{conv}} \sum_i w_{up}(i)$ is the averaged updraft speed of parcels over convective columns. This approximation is based on the fact that these parcels in a large number are vertically distributed uniformly so that their mean updraft is proportional to that at a certain level. **?** assumed a constant value of w^*_{up} and concluded that its magnitude determines the final state of mesoscale clusters in the multi-column model. Considering the fact that the convective column number N_{conv} is coupled to

the parcel dynamics, we recognize the value of w^*_{up} as a key parameter to determine the subsidence strength.

c. Input data for environmental profiles

Two datasets are used in this study to assess the environmental profiles in current and future climate. To discuss the initiation of summertime MCSs over the U.S., we focus on the 14-year (2004-2017) summer-time (June-August) data over a domain slightly larger than the contiguous U.S. ($20^\circ - 55^\circ$N, $130^\circ - 65^\circ$W). We choose this 14-year period to be consistent with **?**. The first dataset is from the fifth generation ECMWF reanalysis (ERA5) hourly data product (**?**) and downloaded from the Climate Data Store (CDS) website (`https://cds.climate.copernicus.eu/cdsapp#!/dataset/reanalysis-era5-pressure-levels?tab=form`). The original $0.25^\circ \times 0.25^\circ$ resolution data is further coarse-grained onto the $1^\circ \times 1^\circ$ grid spacing, the latter of which serves as local environmental profiles for the Lagrangian parcel model. The climatological mean environmental profiles are also used as initial sounding for those SAM simulations as mentioned above. It has been shown that ERA5 successfully reproduces severe local storm environments with strong spatiotemporal correlations and low biases, especially over the Great Plains (**?**). These hourly ERA5 profiles of temperature and specific humidity are used as input in both single- and multi-column models to simulate the current climate. The second dataset is the monthly temperature and specific humidity anomalies between future climate (2056-2099; RCP8.5) and current climate (1962-2005; historical) based on 37 CMIP5 models (**?**). This dataset is used to assess how changes of the environmental thermodynamic profiles under global warming may influence the convective initiation and genesis of summertime MCSs over the U.S.

d. Experiment setup details

The Lagrangian parcel model describes the rising trajectory of a buoyancy-driven parcel, providing a useful tool in assessing the convective activity response to the input environmental profile. For future climate under global warming, we use the PGW approach where the future hourly environmental profile is approximated by the ERA5 hourly environmental profile in current climate plus a climate perturbation derived from GCM ensemble projection of mean climate change. In this study, we conduct 6 sets of experiments in total based on the single- and multi-column models. The

TABLE 2. Setup details for all the experiments conducted in this study. From left to right, the columns are for (#) experiment index, (Model) single- or multi-column Lagrangian parcel model, (Environmental profile) the temperature and moisture profiles used to drive the model, (Simulation Count) total number of simulations, (Figure) figures for the corresponding results, (Description) the purpose of the experiment. The "future climate perturbation" is calculated as the mean state difference between future climate (2056-2099; RCP8.5) and current climate (1962-2005; historical) based on 37 CMIP5 model projections. The "current climate model bias" is calculated as the summer mean state difference between CMIP5 models and ERA5 data for the period (1996–2005). The U.S. domain is 130°W–65°W, 20°N–55°N, and the central U.S. domain is 100°W–90°W, 35°N–45°N. All multi-column model simulations have four ensemble members with only differences in random initiation conditions.

#	Model	Environmental profile	Simulation Count	Figure	Description
1	single-column	current profile = 2004–2017 JJA ERA5 hourly data over the U.S., Future profile = current profile + future climate perturbation	$2 \times (24 \times 92 \times 14) \times (65 \times 35) \approx 1.4 \times 10^8$	Fig. 3g-h, 5, 6, 7a	impact of global warming on convective initiation
2	single-column	current profile = 2004–2017 JJA ERA5 hourly data over the U.S. + current climate model bias, future profile = current profile + current climate model bias + future climate perturbation	$2 \times (24 \times 92 \times 14) \times (65 \times 35) \approx 1.4 \times 10^8$	Fig. 4d-f	impact of current climate mean state model bias on future projection
3	multi-column	climatological mean (2004–2017 JJA) ERA5 data averaged over central U.S., moisture profile is multiplied by 1.0, 1.1, 1.2	$2 \times 3 \times 4 = 24$	Fig. 8	effects of parameterized gust front propagation speed and subsidence strength on convection aggregation
4	multi-column	current profile = specific ERA5 hourly data averaged over central U.S., future profile = current profile + future climate perturbation	$5 \times 4 = 20$	Fig. 9	impact of global warming on MCS genesis in four different global warming scenarios
5	multi-column	current profile = specific ERA5 hourly data averaged over central U.S., future profile = current profile + future climate perturbation	$3 \times 2 \times 4 = 24$	Fig. 10	additional three cases with different environmental profiles for sensitivity experiments

setup details for all the experiments are summarized in Table 2. In all single-column experiments (#1, #2), the initial condition $\delta q = 0\ g/kg$ and $\delta z = 2.5\ km$ are used throughout the US domain in both current and future climate scenarios. In all multi-column experiments (#3, #4, #5), the initial condition $\delta q = 3\ g/kg$ and $\delta z = 0$–$2.5\ km$ along with the central U.S. environmental profiles are used in both current and future climate scenarios.

Experiment 1 consists of two sets of single-column model simulations (one for current climate and the other for future climate) and is used to assess the impact of global warming on convective initiation. For each 1deg-by-1deg grid over the U.S. domain (130°W–65°W, 20°N–55°N), the single-column model is run multiple times and driven by ERA5 hourly environmental profiles

(full pressure-level temperature and specific humidity) during the 14-year summertime period (2004–2017 JJA). That is, a total of $2 \times 24 \times 92 \times 14 = 61824$ simulations are conducted for each 1deg-by-1deg grid. The environmental profiles used to drive the model reads as follows,

Current profile = ERA5 hourly data

Future profile = ERA5 hourly data + future climate perturbation

where the future climate perturbation (full pressure-level temperature and specific humidity) is the mean state JJA difference between future climate (2056-2099; RCP8.5) and current climate (1962-2005; historical) based on 37 CMIP5 model projection. To reconcile the inconsistency in horizontal and vertical resolutions between ERA5 and CMIP5, we first interpolate the CMIP5 data onto the same grids as the ERA5 through the spline interpolation method.

Experiment 2 is similar to experiment 1 except that both current and future profiles are modified by adding a current climate model bias,

Current profile = ERA5 hourly data + current climate model bias

Future profile = ERA5 hourly data + current climate model bias + future climate perturbation

where the current climate model bias is calculated as the mean state difference between CMIP5 models and ERA5 data for the period (1996–2005 JJA). Here we choose this 10-year period that does not overlap with the 14-year period (2004–2017 JJA) to match the CMIP5 historical runs that only cover the period 1962–2005.

Experiment 3 is used to assess the effects of parameterized gust front propagation speed and subsidence strength based on the multi-column model, driven by the climatological mean (2004–2017 JJA) ERA5 environmental profiles averaged over central U.S. (100°W–90°W, 35°N–45°N). We considered 3 cases with their moisture environmental profiles multiplied by 1.0, 1.1, 1.2, respectively. For each case, 4 ensemble simulations with only difference in initial random conditions are conducted for the sake of robustness.

Experiment 4 consists of 5 sets of multi-column model simulations for 5 different scenarios, including the current climate scenario and 4 different global warming scenarios for future climate. The current environmental profile used to drive the model is based on a specific ERA5 hourly data averaged over the central U.S. at 5 UTC, July 17, 2013. The future environmental profile is equal to the current environmental profile plus the future climate perturbation as mentioned above.

Experiment 5 is similar to experiment 4, except that their environmental profiles are selected for different times of the day and different dates over the central U.S., including i) 18 UTC, June 2, 2014, ii) 4 UTC, August 28, 2017, iii) 19 UTC, June 30, 2016. This experiment is used to assess the sensitivity of model results to environmental profiles.

3. Impact of global warming on convective initiation: results from the single-column model

Convective initiation is the early stage of MCS initiation where scattered convection are triggered due to either dynamical lifting or thermodynamic favorable conditions. **?** showed that the single-column Lagrangian parcel model captures readily the basic features of a rising parcel, demonstrating the collective effects of boundary layer moistening and dynamical lifting in triggering convective initiation and reproducing successfully its early afternoon peak over the central U.S. in the observation. In general, the single-column model describes the response of convective initiation to the background thermodynamic fields in temperature and moisture. Here we use the single-column model to study the convective initiation stage in general, no matter whether it leads to MCS genesis eventually. The goal of this section is to investigate the skills of this model in capturing climatological mean precipitation and convective population in current climate and its ability to reproduce the future mean precipitation and convective population projected by the CMIP models. As motivated by the common climate model biases in simulating precipitation and surface temperature in the central U.S., we also discuss the impact of current climate mean state model bias in predicting future climatological mean precipitation. The initial moisture of the parcel is set to be the same as the environmental air ($\delta q_v = 0$) and dynamical lifting distance δz is 2.5 km for all simulations in this section. The choice of these initial conditions are used to mimic the favorable conditions for convection due to dynamical lifting effects δz from eastward-moving large-scale environments and subsynoptic perturbations (**?????**). The moisture anomaly δq_v is set to zero to mimic the local thermodynamic favorable condition for convection for the sake of simplicity.

a. Changes in climatological mean precipitation

Fig. 3 shows the climatological mean spatial distributions of summertime surface temperature, moisture, and precipitation in the current climate and the future change under global warming. In the observed current climate, surface temperature exhibits a clear east-west contrast with its

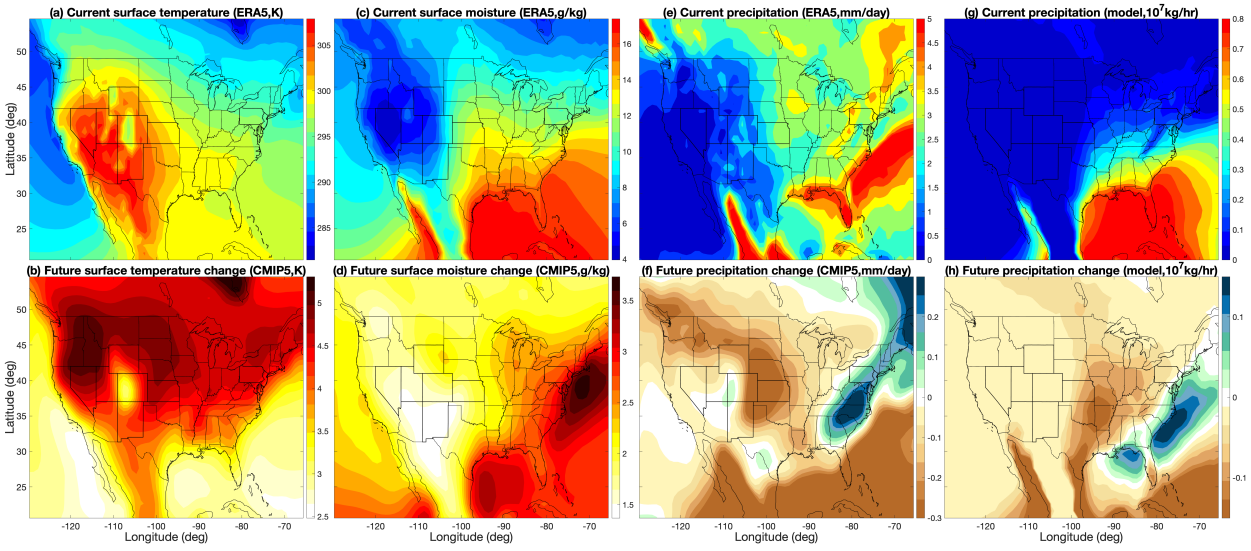

460 FIG. 3. Comparisons of climatological mean summertime precipitation and its future change between the
461 single-column model results and 37 CMIP5 model projections. Panel (a) shows climatological mean surface
462 temperature based on 2004-2017 June-July-August (JJA) ERA5 data, while panel (b) show future mean surface
463 temperature change between future climate (2056-2099; RCP8.5) and current climate (1962-2005; historical)
464 based on 37 CMIP5 models. Panels (c,d) and (e,f) are similar to panels (a,b) but for surface moisture and
465 precipitation, respectively. Panel (g,h) are similar to panel (e,f) but based on the single-column model, where
466 the value (color shading) indicates the accumulated precipitation amount within the 1-h simulation duration for
467 each $1deg \times 1deg$ grid. The pattern correlation between panels (e) and (g) is 0.49, and that between panels (f)
468 and (h) is 0.57.

472 maximum over the western and central U.S. in panel (a), while surface moisture peaks to the south
473 over the southeastern U.S., the Gulf of Mexico, the Atlantic ocean, and the Pacific coast of Mexico
474 in panel (b). The future surface temperature increase projected by CMIP5 models is manifested
475 by large warming anomalies over North America with its maximum over the Pacific Northwest in
476 panel (b). The future surface moisture increase is much weaker over land than ocean, consistent
477 with the land aridity effect (**?**), as shown in panel (d).

478 By incorporating the hourly 1deg-by-1deg ERA5 temperature and moisture as background en-
479 vironmental profiles, the single-column model estimates theoretically the climatological mean
480 precipitation amount in panel (g) with its maximum over the southeastern U.S., the Atlantic ocean,
481 and Pacific coast of Mexico. This spatial pattern matches well with that based on the ERA re-

analysis data in panel (e). The underestimated precipitation over the northeastern U.S. and Canada is presumably due to the absence of ice-phase processes in the simple model. By adding the future temperature and specific humidity mean changes from the CMIP5 projections to the ERA5 hourly environmental profiles, the single-column model projects precipitation decreases over the central U.S., Pacific coast of Mexico, and the Atlantic ocean, and precipitation increases along the eastern coast of the U.S. in panel (h), resembling those projected by the CMIP5 models in panel (f). Overall, these similar spatial patterns between the single-column model results, ERA5 reanalysis data, and CMIP5 model projections demonstrate the skills of the simple theoretical model in capturing the climatological mean precipitation pattern and highlight the crucial role of environmental thermodynamic fields in controlling the mean state of convection and its future changes. That said, there also exist several differences among these fields, including the large moist bias in the subtropical ocean and a generally dry bias in most of the inland region in panel (g), and the eastward displacement of the moistening response over the ocean areas in panel (h). This is partly due to the missing dynamical fields in the simple-column model. For example, vertical wind shear is an important controlling factor modulating the convective storms at midlatitudes. Although the spatial pattern of current precipitation and future precipitation change provide us many interesting insights, it is inappropriate to directly compare the absolute value of precipitation amount in the same unit between panels (e,f) and (g,h). Notably, a larger/smaller initial parcel volume (currently $10^9 m^3$) would result in larger/smaller precipitation amount, but not change the spatial patterns in panels (g,h). Also, the rain falling out from a plume may not be equal to the rainfall amount in a GCM grid box. To distinguish these differences, we leave the precipitation unit (mm/day) in panels (e,f) to be different from that (kg/hr) in panels (g,h).

b. Current climate mean state model bias

The state-of-the-art climate models exhibit significant biases in simulating the mean state of the atmosphere as shown in Fig. 4a-c. Compared with ERA5 reanalysis data, the CMIP5 models have significant warm biases over the central U.S. and along the Pacific coast of North America, and cold biases over the Pacific northwest in panel (a). Besides, the surface moisture in the CMIP5 simulations in panel (b) is underestimated in the southern U.S., the Atlantic ocean and the Sierra Madre Occidental, but overestimated in the Pacific northwest, the Pacific coast and central Mexico.

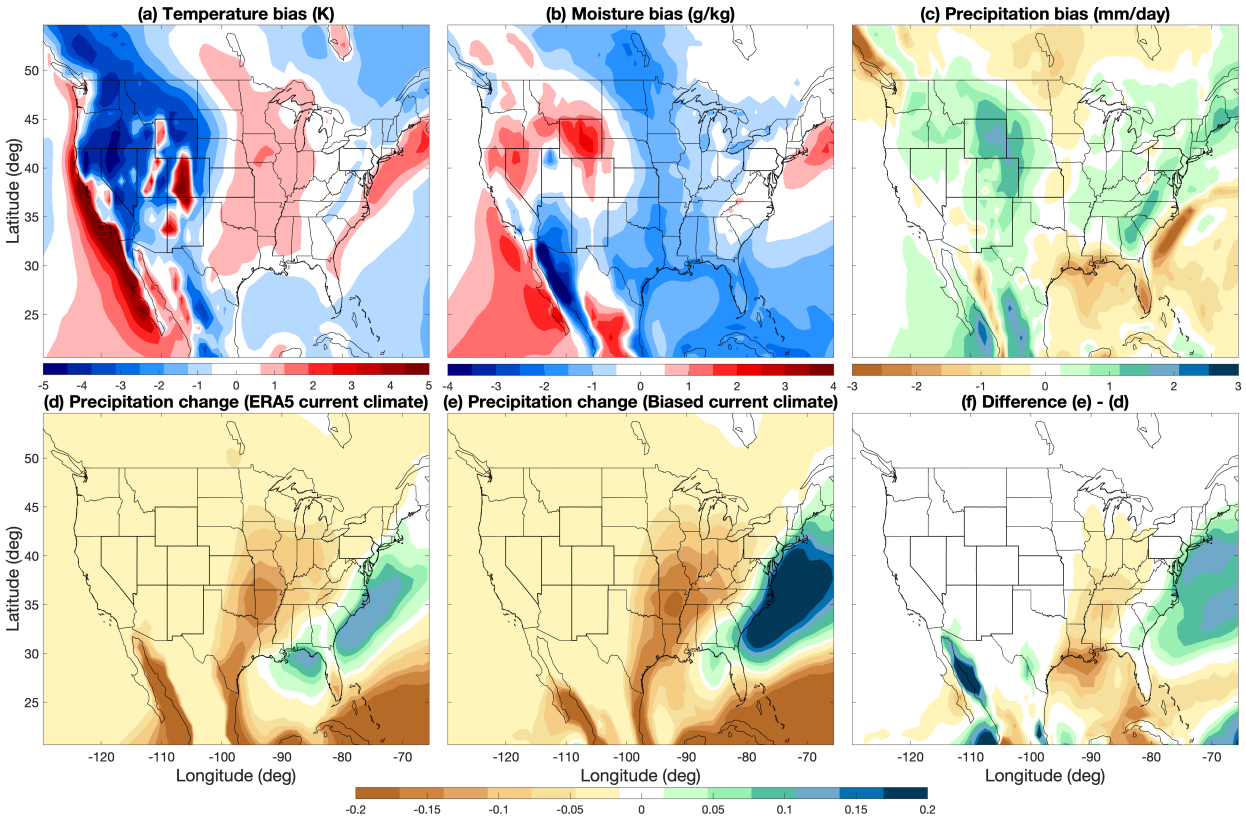

FIG. 4. Biases of climatological mean fields of (a) surface temperature, (b) surface moisture, and (c) precipitation in CMIP5 model relative to the ERA5 data for the 10-year period (1996–2005). Panel (d) shows the future mean precipitation change (unit: $10^7\ kg/hr$) predicted by the single-column model (the same as Fig. 6h). Panel (e) is similar to panel (d) except that each hourly current environmental profile is modified by adding the mean state biases in temperature and moisture (panel a,b). Panel (e) shows the difference between panels (e) and (d).

Furthermore, slight dry biases are found over the central U.S., while wet biases are seen in the Pacific northwest and western Mexico. It is important to determine how these biases in current climate mean state could influence the model projection for future precipitation change. Fig. 4d-f shows such an assessment of climate model projection bias based on the single-column model. Compared with panel (d) which is identical to panel (f) of Fig. 3, the future precipitation change based on the biased current climate environmental profiles in panel (e) overestimated the precipitation decrease over the central U.S. and precipitation increase to the east. Their difference map in panel (f) reaches its magnitude as large as 25% of that in panel (d), reflecting the impact of the large warm and dry biases over the central U.S. in amplifying the projected changes in precipitation. Such a result

also indicates the nonlinear nature of thermodynamic environmental profiles as a controlling factor in determining convection frequency and intensity. Besides the surface field biases, it is worth mentioning that CMIP5 biases at higher levels of the free troposphere may also affect results by modulating atmospheric instability (**?**).

c. Changes in convective population

Based on the simple model output driven by different environmental profiles, we proceed to study the changes in convective population between current climate (ERA5 data) and future climate (PGW approach). Below convective population is categorized in terms of total precipitation amount or final height of the parcel.

Fig. 5 shows the change of convective population over the central U.S. under global warming, as predicted by the single-column model. Here we define different precipitation events in terms of their precipitation amounts, including suppressed convective events (0–$3\times10^6\ kg/hr$), weak precipitation events (3–$9\times10^6\ kg/hr$), moderate precipitation events (9–$15\times10^6\ kg/hr$), and strong precipitation events > $15\times10^6\ kg/hr$). It is worth noting that the suppressed convective events typically correspond to a scenario where the parcel does not rise to upper levels and only releases negligible precipitation amount. As shown by panel (a), the convective population based on precipitation amount features a bimodal distribution with its first peak at zero and the second peak near $12\times10^6\ kg/hr$. For larger precipitation events, their frequency drops dramatically as the precipitation amount increases beyond $12\times10^6\ kg/hr$. In contrast, the convective population in future climate has reduced frequency for events with precipitation amount less than $14\times10^6\ kg/hr$ but increased frequency for those events larger than that. This result is consistent with convection-permitting regional climate simulations of **?** that weak to moderate convection will decrease and strong convection will increase in frequency in the future climate. The scatter plot in panel (b) indicates that in future climate, the majority of moderate and strong convection is further enhanced by $2\times10^6\ kg/hr$, and a fraction of weak convection is enhanced more than $2\times10^6\ kg/hr$. Meanwhile, a fraction of weak to moderate to strong convection is reduced or even suppressed, presumably due to increased convective inhibition. A parallel analysis based on the parcel final height in panels (c) shows similar results with reduced weak and moderate convection and increased strong convection. The scatter plot in panel (d) confirms that the majority of deep convection with

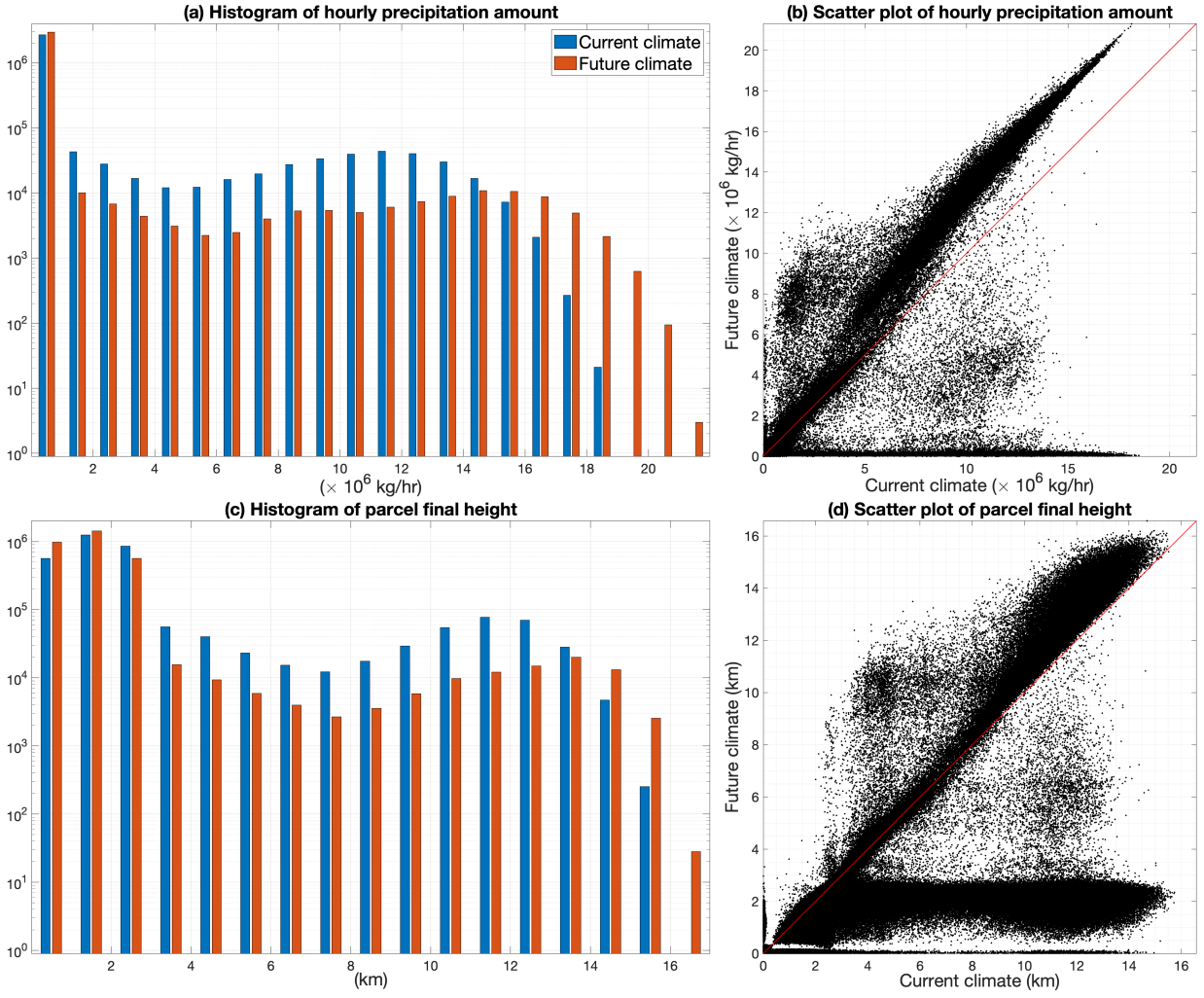

534 FIG. 5. Convective population shifting over the central U.S. (35° – 45°N, 100° – 90°W) due to global warming,
535 predicted by the single-column model. Panels (a-b) are the histogram and scatter plot for hourly precipitation
536 amount, while panels (c-d) are for final height of the parcel. The overlaid red lines in panels (b,d) indicate the
537 scenario when precipitation/final height in current and future climate are the same.

558 final height more than 10 km is enhanced the most, while convection suppression occurs throughout
559 all convection categories.

565 To further examine the change of convection population, Fig. 6 shows the spatial distributions
566 of frequency changes in all six convection categories in terms of precipitation amount. Overall,
567 the single-column model predicts reduced weak and moderate convection and increased strong
568 convection over the North America, consistent with the high-resolution convection-permitting

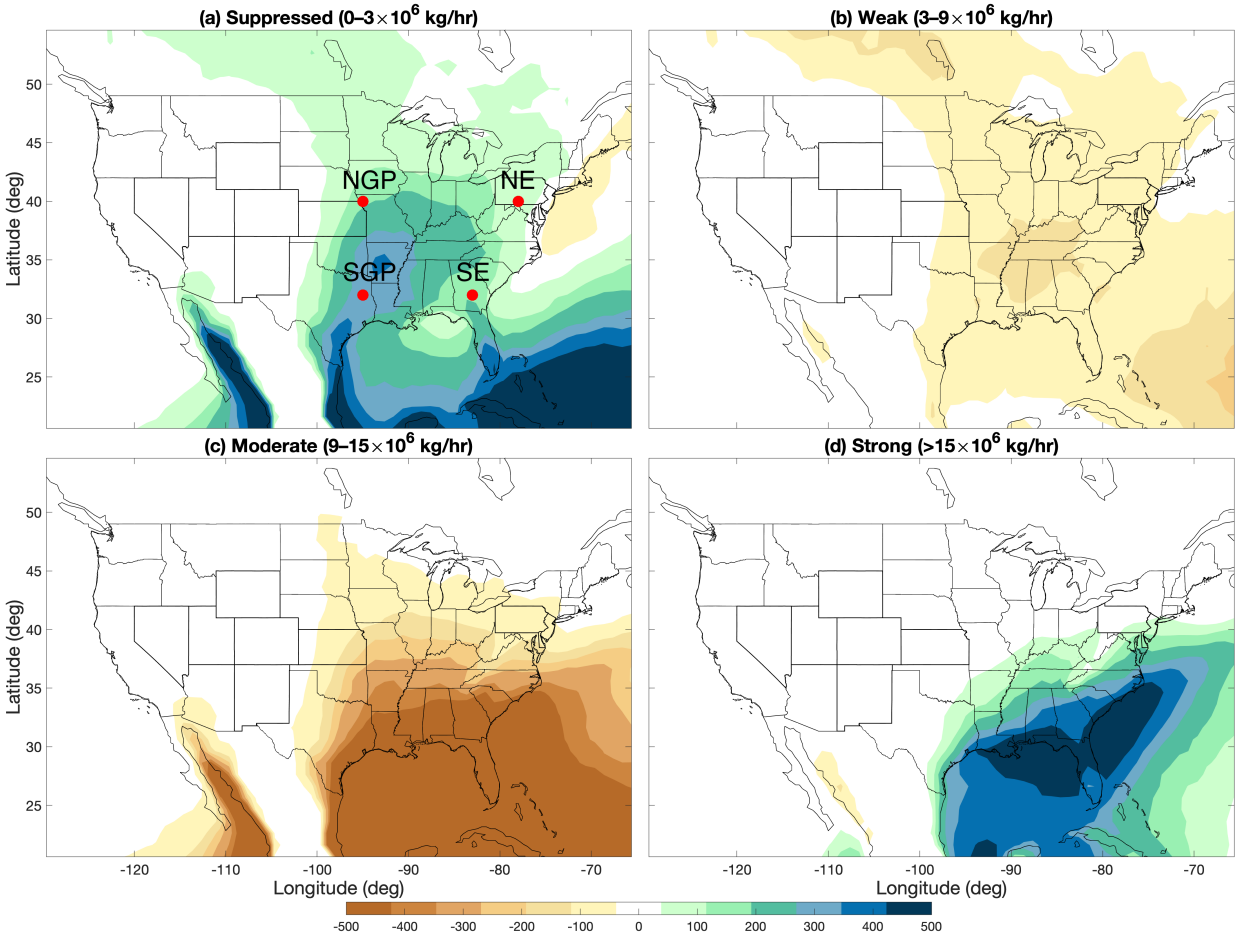

560 FIG. 6. Difference maps of occurrence of JJA precipitation events between future and current climate predicted
561 by the single-column model. These panels correspond to six different precipitation amount categories, including
562 (a) suppressed convective events ($0–3\times10^6\ kg/hr$), (b) weak precipitation events ($3–9\times10^6\ kg/hr$), (c) moderate
563 precipitation events ($9–15\times10^6\ kg/hr$), (d) strong precipitation events ($>15\times10^6\ kg/hr$). The yellow circles
564 in panel (a) indicate the four representative grid points we selected for detailed analysis in Fig. 7.

569 regional climate simulations of **?**. In details, the suppressed convective category in panel (a) has
570 increased frequency over the eastern and central U.S., the Atlantic ocean, and the Pacific coast
571 of Mexico, reflecting the reduced total convection frequency there under the global warming.
572 The weak convection categories in panels (b,c) have reduced frequency over the eastern U.S.,
573 the Atlantic, and the southern Canada. The moderate convection categories in panels (d,e) have
574 reduced frequency mostly over the southeastern U.S. and the Atlantic ocean, while strong convection
575 category in panel (f) exhibits increased frequency over the similar regions. These results reflect

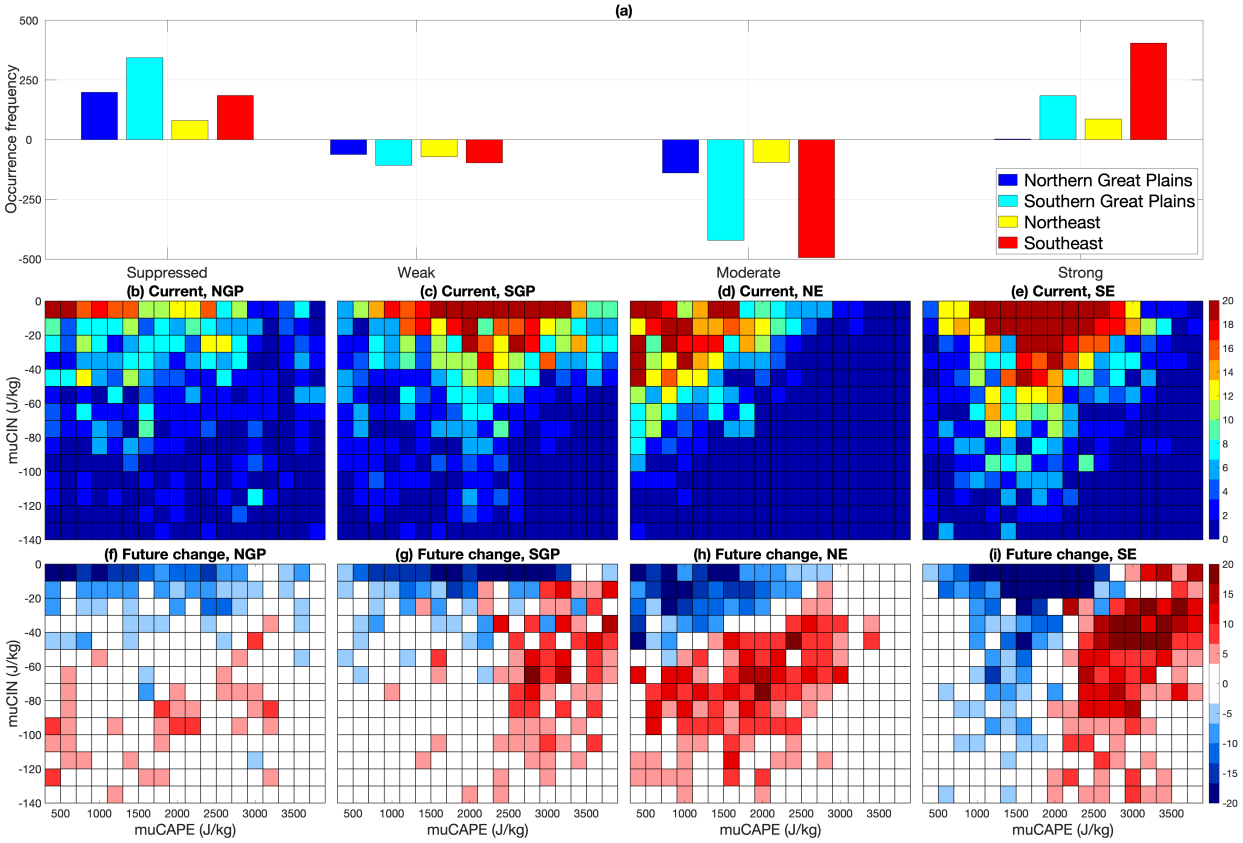

FIG. 7. Panel (a) shows the histogram for 14-year mean JJA occurrence changes of different precipitation events over four 1deg-by-1deg regions (indicated by the yellow circles in Fig. 6a), predicted by the single-column model. Panel (b) shows the 2D histogram for most unstable CAPE (muCAPE) and most unstable CIN (muCIN) associated with the 2004 JJA hourly environmental profiles over the Northern Great Plains in current climate, while panel (f) shows its future change under the warming. Panels (c,g), (d,h),(e,i) are similar to panels (b,f) but for Southern Great Plains, Northeast, Southeast regions.

the usefulness of the single-column model to infer the future change of convection population and highlights the different response of convective population to the global warming.

To understand the essential reason for the spatial distribution of mean precipitation changes in Fig. 6, we select four 1deg-by-1deg grid points over the Northern Great Plains (NGP), Southern Great Plains (SGP), Northeast (NE), and Southeast (SE), respectively, for detailed analysis. Fig. 7a shows the histogram for JJA mean occurrence changes of different precipitation events over these four regions, which is generally characterized by decreased weak and moderate precipitation events,

increased strong precipitation events, and increased suppressed convective events. The increased occurrence frequency of suppressed convective events reflects the decreased total occurrence frequency of convective events. In particular, the NGP region is featured by slightly less occurrence of weak and moderate precipitation events but almost no changes in strong precipitation events, leading to a mean precipitation decrease as seen in Fig. 3h. In contrast, the SE region is featured by much less occurrence of weak and moderate precipitation events and more occurrence of strong precipitation events, leading to a mean precipitation increase. A further analysis based on these hourly environmental profiles in panels (b-i) indicates increased most unstable CAPE (muCAPE) over the SGP, NE, and SE regions and increased most unstable CIN (muCIN) over all four regions, promoting strong convection and suppressing weak and moderate convection respectively. In particular, the NGP region is dominated by small muCAPE and large muCIN events, while the SE region has more occurrence of large muCAPE events. Due to expensive computation, here we only calculate the muCAPE and CIN in the year 2004 as an example.

4. Impact of global warming on MCS genesis: results from the multi-column model

? further developed a multi-column model by including an array of single-column models aligned in the east-west direction and incorporating idealized cold pool interaction mechanisms. The multi-column model captures readily the cold pool-induced upscale growth feature in MCS genesis. The goal of this section is to investigate the impact of global warming on the final state of mesoscale clusters in the multi-column model. To achieve that, we first develop the parameterization of gust front propagation speed and subsidence strength under the guidance of cloud-resolving simulations in Section 2b. Then we demonstrate how these two factors control the upscale growth of mesoscale clusters in the presence of different background moisture profiles. Finally, we use this improved version of the multi-column model to investigate the change of MCS genesis under global warming in various possible scenarios. The sensitivity of model results to environmental profiles is also discussed. The initial moisture anomaly δq_v of all parcels is set as $3g/kg$, and their dynamical lifting distance δz is uniformly distributed in equal probability between 0 and 2.5 km for all simulations in this section. In contrast to the initial condition $\delta q_v = 0$ for convective initiation in the last section, we consider a positive the moisture anomaly δq_v here to mimic the thermodynamic favorable condition for MCS genesis, resulting from the accumulation

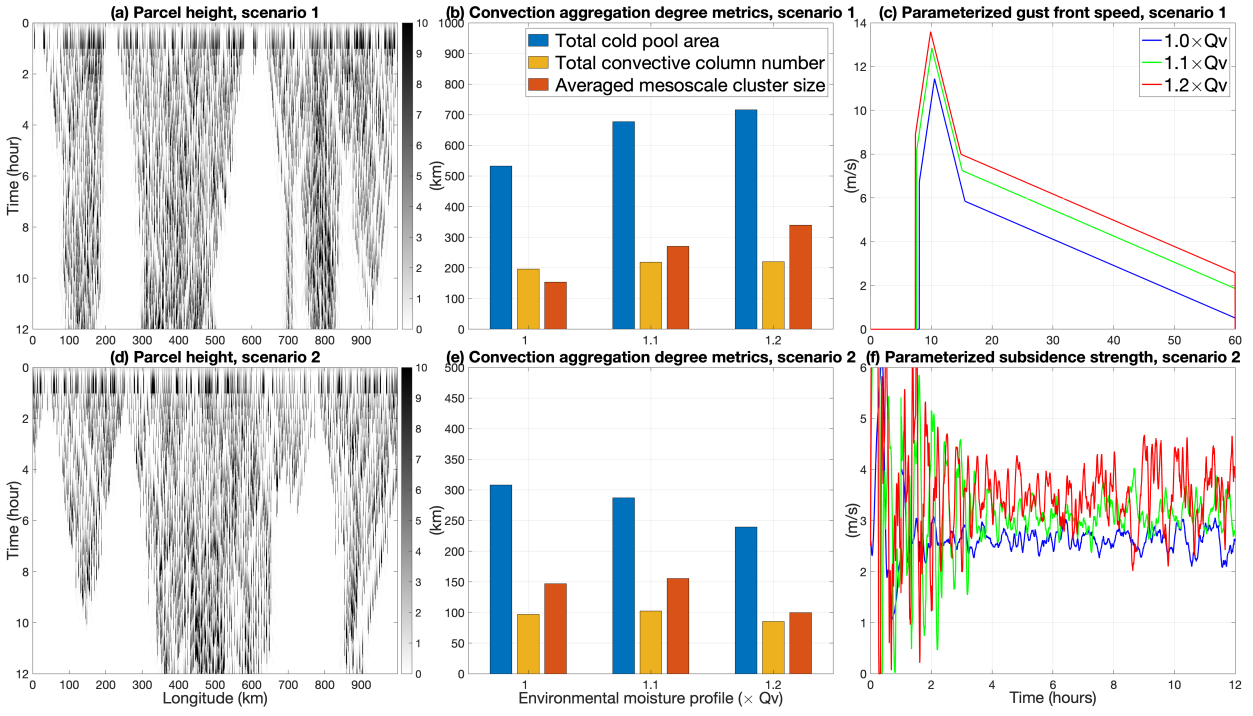

621 FIG. 8. Multi-column model simulations in two different scenarios, (a-c) with parameterization of gust front
622 propagation speed and fixed subsidence strength, (d-f) with fixed gust front propagation speed and parameteriza-
623 tion of subsidence strength. In either of these two scenarios, three cases with the same environmental temperature
624 profile but different environmental moisture profiles (multiplied by 1.0, 1.1, 1.2, respectively) are considered.
625 Panels (a,d) show the Hovmöller diagrams for parcel height (unit: km) in specific ensemble simulations with
626 $1.0 \times Qv$ environmental moisture profile. Panels (b,e) show the bar diagrams for three convection aggregation
627 degree metrics in the three cases with different moisture profile. Panel (c) shows the parameterized gust front
628 propagation speed in the first scenario, while panel (f) shows the time series of parameterized updraft speed for
629 subsidence strength parameterization in the second scenario.

618 of moisture around the edges of cold pools (**?**). The distribution of δz introduces randomness in
619 the initial condition, mimicking the scattered convection before the MCS genesis.

620 *a. Dependence of MCS genesis on gust front propagation speed and subsidence strength*

630 Fig. 8a shows the Hovmöller diagram for parcel height from the multi-column model with the
631 parameterized gust front propagation speed and fixed subsidence strength. Overall, all parcels
632 are initiated from a random distribution and gradually aggregate into mesoscale clusters after a

few hours, resembling the upscale growth features during MCS genesis (**?**). By increasing the background moisture profile from $1.0 \times Q_v$ to $1.2 \times Q_v$, both total cold pool area and averaged mesoscale cluster size increase in panel (b), while total convective column number stays the same. A further investigation in panel (c) shows that this is due to the increasing gust front propagation speed in the parameterization. In general, the wetter background profile provides more favorable conditions for convection, promoting larger accumulated surface rainfall. The resulting faster propagation speed in Eqs. 1-2 means the gust front propagates further away from the convection, expanding the cold pool area as well as mesoscale cluster size. On the other hand, the faster propagating gust front spends less time and introduces less lifting effects at each column as it passes by, offsetting the effects of cold pool expansion. Similar upscale growth feature is also seen in Fig. 8d with the fixed gust front propagation speed and parameterized subsidence strength. By increasing the background moisture profile from $1.0 \times Q_v$ to $1.2 \times Q_v$, all three aggregation degree metrics decrease in panel (e). The slight increase of total convective column number and averaged mesoscale cluster size in the $1.1 \times Q_v$ case is presumably related to the uncertainty from random initial conditions in the 4-ensemble member simulations. A further investigation in panel (f) shows that this is mainly due to the stronger subsidence strength in the wetter cases so that more convection is suppressed. This result highlights the crucial role of gust front propagation speed and subsidence strength in determining the final state of mesoscale cluster in the multi-column model.

b. Impact of global warming on MCS genesis in various scenarios

To assess the impact of global warming, we compare the multi-column model output by switching the environmental profiles from current to future climate, turning on both the gust front propagation speed and subsidence strength parameterizations. Besides current climate (Current) and future climate (GW), we also consider another three scenarios in the future climate, including one with more favorable conditions for convection (GW+Favorability), one with long convection duration (GW+Duration), and one with stronger cold pool lifting effect (GW+Lifting). To implement them in the multi-column model, we increase the initial moisture anomaly from 3 g/kg to 9 g/kg in scenario GW+Favorability, extend the parcel lifetime from 1 hr to 1.5 hr in scenario (GW+Duration), and double the lifting distance by both cold pool collision and spreading in scenario (GW+Lifting).

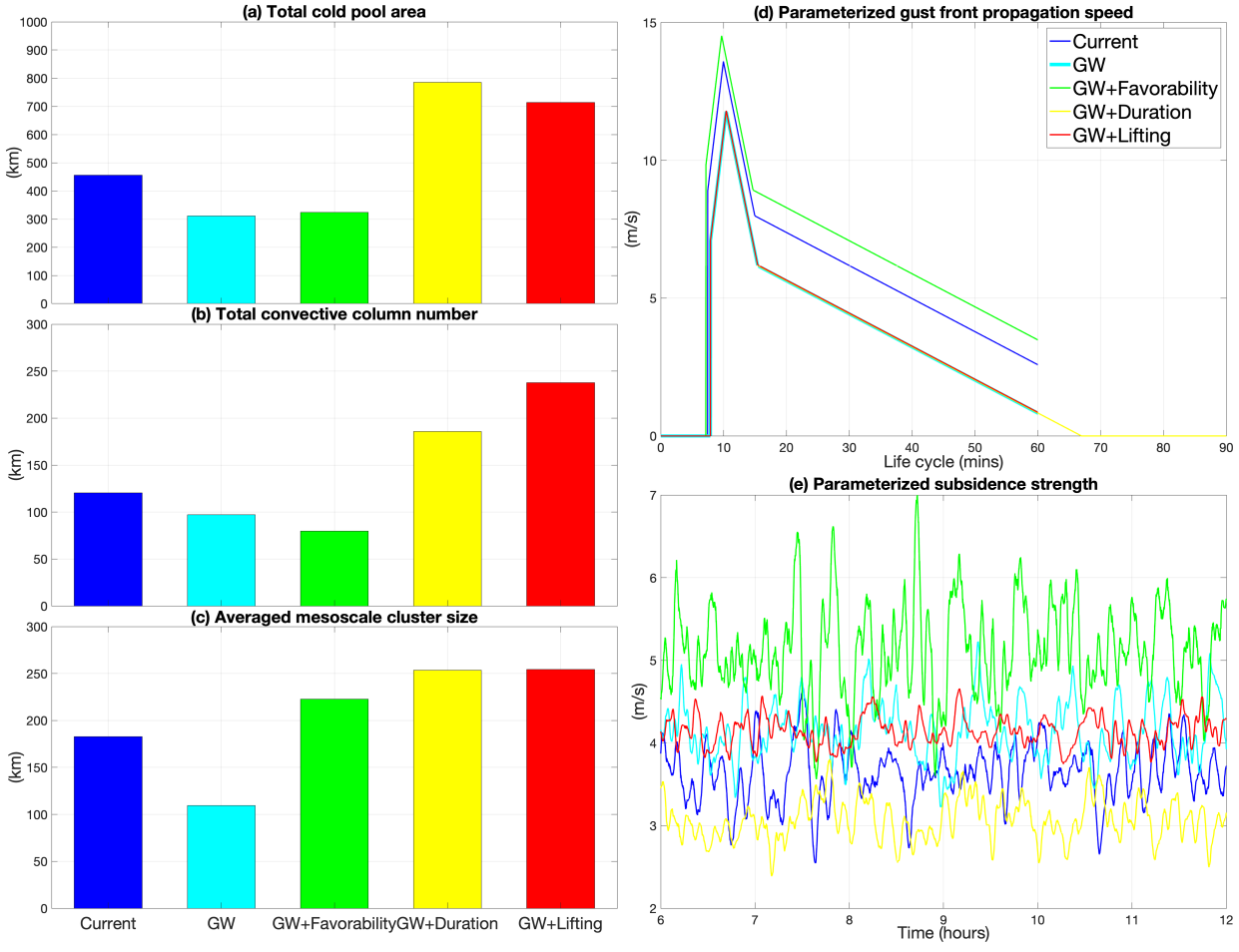

FIG. 9. Multi-column model simulations with both parameterizations of gust front propagation speed and subsidence strength in five different scenarios, including one for current climate and the other four for future climate under global warming. Panels (a-c) shows the bar diagrams for three convection aggregation metrics respectively, including (a) total cold pool area, (b) total convective column number, (c) averaged mesoscale cluster size. Panel (d) shows the parameterized gust front propagation speed in these five scenarios, while panel (e) shows the time series of parameterized updraft speed for subsidence strength parameterization.

Fig. 9a-c summarizes the aggregation degree of convection in these 5 scenarios, and Fig. 9d-e show the corresponding gust front propagation speed and subsidence strength. When compared with the scenario Current (blue), all three aggregation degrees including total cold pool area, total convective column number, and averaged mesoscale cluster size decrease in the scenario GW (cyan). It turns out that the parameterized gust front speed is reduced and subsidence strength is enhanced in the future climate, both of which provide unfavorable conditions for MCS genesis (**?**).

This change is attributed to the increasing CAPE and CIN under global warming (**?**). Due to land aridity and reduced relative humidity under global warming, the increasing CIN leads to reduced initial buoyancy for the parcel so that the initial accumulated surface precipitation is smaller. Also, the gust front propagation speed largely depends on accumulated surface precipitation (see Eqs. 1-2), resulting in slower speed in future climate. Note that the total precipitation amounts in both the Current and GW scenarios are shown in Fig. 10b. On the other hand, the subsidence strength is determined by the averaged updraft speed (see Eq. 5). Due to the larger CAPE in future climate, the updraft speed of parcel typically becomes faster in the later stage of its life cycle.

Here we also investigate three other possible scenarios under global warming. While on average parcels over the land become drier due to the increased land aridity (reduced relative humidity) under the global warming, regional changes in circulation may still provide favorable conditions for convection. For example, **?** found that the frequency of Great Plains low-level jet related environments favorable for MCS initiation will increase by 65% under a high emission scenario, which could increase dynamical lifting by wind convergence in the exit region of the low-level jet. The scenario GW+Favorability (green) mimics more favorable conditions for convection, which may occur in environments strongly influenced by atmospheric moisture transported from the ocean or under favorable soil moisture conditions and enhanced evapotranspiration from the surface (**?????**). Fig. 9a-c indicates that both total cold pool area and convective column number decrease while averaged mesoscale cluster size increases, resulting from the competing effects of the faster gust front propagation speed in panel (d) and stronger subsidence strength in panel (e). The scenario GW+Duration (yellow) mimics longer life time of individual convection, presumably due to the larger fraction of stratiform clouds and slower detrainment process under global warming. It turns out that all three aggregation degree metrics increase in this scenario, partly due to weaker subsidence strength in panel (e). Meanwhile, the longer duration of convection allows further propagation distance of gust fronts, favoring cold pool expansion and triggering more new convection in the neighboring regions. Lastly, the scenario GW+Lifting (red) mimics stronger mechanical lifting effects from cold pool expansion and collision, presumably due to more intense precipitating events under the global warming. This stronger lifting effect leads to an increase in all three aggregation degree metrics in Fig. 9a-c, although both gust front propagation speed and subsidence strength are the same as the scenario GW. In this model, the GW+Lifting scenario is

achieved by increasing the magnitude of both lifting effects σ_{iso} and σ_{col}. In reality, the actual lifting effect depends on virtual temperature gradient at the head of the gust front. For example, a bigger initial moisture anomaly for the parcel would produce higher precipitation intensity, creating stronger cold pool gust fronts as well as their lifting effects. When compared with the scenario GW, all the other three GW scenarios shows tremendous increase in averaged mesoscale cluster size, and the scenarios GW+Duration and GW+Lifting also show significant increase in total cold pool area and total convective column number. Overall, these three additional global warming scenarios demonstrate different outcomes compared to the scenario GW (e.g., increased rather than decreased mesocale cluster size with warming), highlighting those factors (convective environments, convection duration, and cold pool lifting effects) in determining the final state of mesoscale clusters in the multi-column model.

It is worth noting that the environmental profiles used in the previous multi-column model simulations is only representative of the mean central U.S. environment at one specific hour. Fig. 10 shows the sensitivity of these multi-column model simulations to the environmental profiles in assessing the impact of global warming, based on four different cases (Case 4 is the one used in the previous simulations). They are selected from environments where future precipitation is higher than current precipitation but at different intensities over the central U.S. The most unstable (MU) CAPE of these four cases ranges from 405.4 J/kg to 1291.4 J/kg, representing typical environmental conditions for weak and strong convection. Besides, the total precipitation amount in current climate (see the first number in Fig. 10b legend) is the largest in Case 4 and the smallest in Case 1, and all the four cases show a total precipitation amount increase under global warming (see the second number in Fig. 10b legend). The corresponding temperature profiles in panel (a) and moisture profile in panel (b) show a warmer and wetter free troposphere in Case 4 than Case 1. Panels (c-d) indicate that Case 4 has slightly faster gust front propagation speed (increase by 0.5 m/s) but much stronger subsidence strength (double) than Case 1. All four cases show a decrease in the three aggregation degree metrics in panel (e), confirming the previous conclusion in the scenario GW. Meanwhile, a direct comparison among these cases show that mesoscale cluster become smaller in an environment with more favorable conditions for convection, consistent with the previous result that stronger subsidence strength tends to suppress MCS genesis (see Fig. 8d-f).

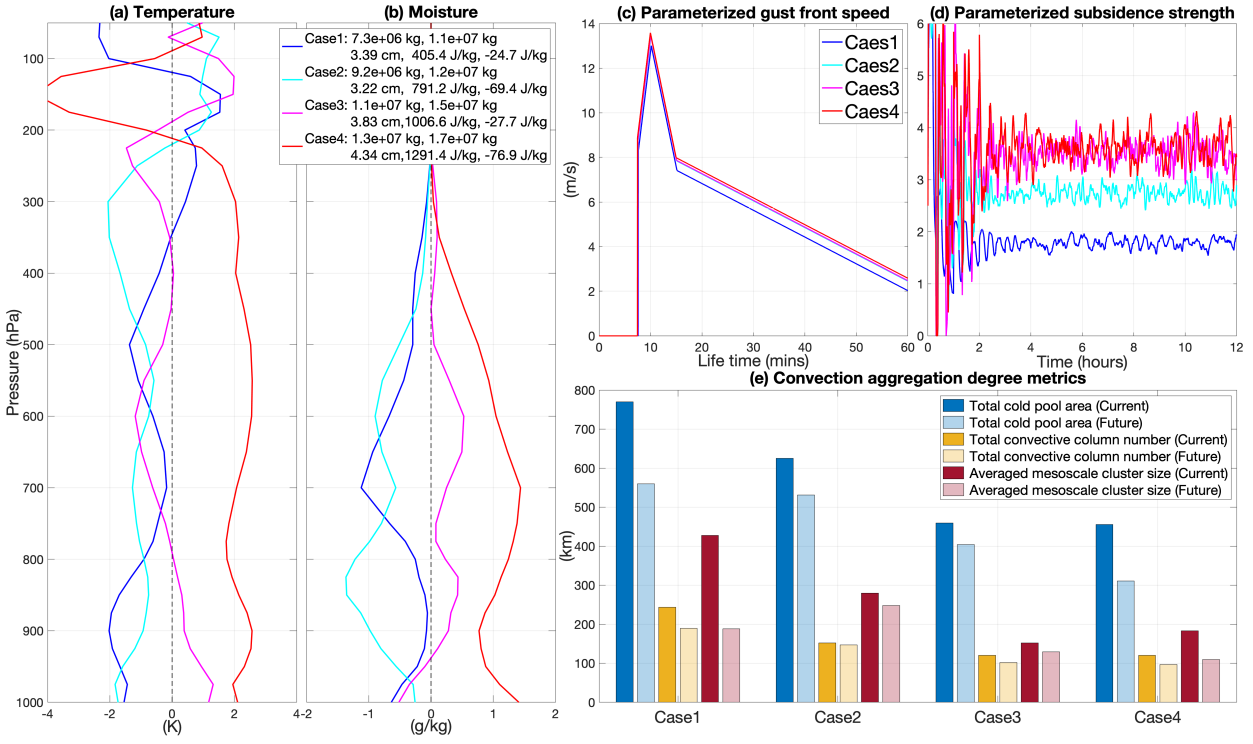

FIG. 10. Multi-column model simulations with both parameterizations of gust front propagation speed and subsidence strength. Four cases with different ERA5 hourly environmental profiles over the central U.S. are considered, where Case 4 is the same as that in Fig. 9. Panels (a,b) show the departure of environmental temperature and moisture in each case from the mean of all four cases. The 5 numbers in panel (b) legend indicates total precipitation amount (based on simple model) in current and future climate, total precipitable water, CAPE, and CIN. Panel (c) shows the parameterized gust front propagation speed in these four cases, while panel (d) shows the time series of parameterized updraft speed for subsidence strength parameterization. Panel (e) shows the bar diagrams for three aggregation degree metrics in these four cases.

5. Discussion and conclusion

This study investigates the impact of global warming on the initiation of summertime MCSs over the U.S., based on a simple Lagrangian parcel model of **?**. The key findings in this study and their linkage with other studies in the literature are summarized and organized for each key finding below.

Single-column model for studying convective initiation As driven by hourly local environmental profiles from current and future climate, the single-column model projects successfully a mean

precipitation decrease over the central U.S. and an increase over the southeastern U.S. in Fig. 3, consistent with the 37 CMIP5 model projection. In particular, the model predicts a mean precipitation increase over the eastern U.S., reflecting a more favorable condition for convection over that region under the global warming. Fig. 7a indicates that the mean precipitation increase over the Northeast region results from increasing frequency of intense precipitation events, which can be intense summertime MCSs and landing tropical cyclones in reality. A further investigation based on this single-column model shows that model bias in simulating the current climate not only increases the magnitude of mean precipitation response but also leads to its eastward shift (Fig. 4). This result points out the major source of uncertainty for GCM future climate projection and urges the need to further narrow down the GCM uncertainty in simulating the current climate. Besides the projected changes in total precipitation, the model also projects a convective population shift with reduced weak to moderate convection and increased strong convection in Fig. 5, suggesting a potential frequency increase in natural disaster and severe weather under global warming. It also shows that such a convective population shifts results from enhanced moderate and strong convection as well as convection suppression in all convection categories in Fig. 6, due to increased CAPE and CIN under global warming (see Fig. 7). Such suppressed summertime precipitation over the central U.S. is also seen in high-resolution (4-km) convection-permitting regional WRF model simulations (**?**), which employ the state-of-the-art microphysics scheme, planetary boundary layer, radiative transfer model, land-surface model as well as realistic initial and boundary conditions. The close match between the single-column model, GCMs, and cloud-resolving regional simulations reflects the skill of the simple theoretical model in capturing the leading-order mean precipitation response to global warming. This convective population shift is consistent with the high-resolution convection-permitting regional simulations (**?**), reflecting the usefulness of the model in assessing convective population response to climate change.

Parameterization development guided by cloud-resolving simulations **?** recognized the key role of gust front propagation speed and subsidence strength in controlling the final state of mesoscale clusters in the multi-column model. To improve their representation in the model, we rely on two sets of cloud-resolving simulations as guidance and develop the corresponding parameterizations based on direct diagnostic analysis and physical law reasoning. Specifically, the parameterization of gust front propagation speed in Eqs. 1-2 consists of two parts, one of which mimics the abrupt

speed boost as the first wave of cold air reaches the surface and the other mimics the gradual slowdown as the cold pool expands. It turns out that the initial accumulated surface precipitation is the key quantity to determine the overall gust front propagation speed in Fig. 1. This is consistent with the physical understanding that cold pool spreading is driven by downdraft mass flux which is correlated with precipitation mass flux. On the other hand, the parameterization of subsidence strength in Eq. 4 is developed based on the conservation law of mass, in agreement with the cloud-resolving simulations in Fig. 2. These two parameterizations are devoted to represent the cold-pool interaction mechanisms, providing a prototype parameterization for incorporating cold pool dynamics in the coarse-resolution GCMs. Similar efforts to track the gust fronts were also reported in previous studies (**??**).

Multi-column model for studying MCS genesis After employing the new parameterization of gust front propagation speed and subsidence strength, we use the improved multi-column model to study the impact of global warming on MCS genesis. It turns out that the environmental temperature and moisture perturbations due to global warming leads to a decrease in the degree of aggregation, which is further attributed to the land aridity induced gust front slowdown and subsidence strength enhancement in Fig. 9. The result here isolates the key response of cold pool interaction mechanisms to global warming through the gust front speed and subsidence strength. It is possible that other environmental factors also play a role in determining the final state of mesoscale clusters in future climate. Thus we further investigate three additional global warming scenarios with more initial parcel moisture anomaly, longer convection lifetime, and stronger cold pool lifting effect. The result confirms the size increase of mesoscale clusters under these global warming scenarios, and illustrates the underlying mechanisms based on the multi-column model. These results explain the potential MCS genesis change under the global warming and point out several important factors for controlling the upscale growth of MCS. The mechanistic processes underpinning the MCS changes under global warming may inform analysis of convection permitting climate change simulations for advancing insights on how convection aggregation may respond to global warming and its role in cloud-radiation feedback. It is worth noting that the high-resolution convection-permitting regional simulations with full physics projects a 20%-70% increase area in heavy rainfall (**?**). In addition, the warm and dry bias that widely exists in current climate models

and convection-permitting models (**????**) may further increase the model uncertainty in projecting the MCS changes under global warming.

Besides reproducing those key features in the reanalysis and CMIP5 projections, this study based on the simple modeling framework also provides some additional knowledge and benefits. First, the simple model itself provides an efficient tool to evaluate environmental profiles for favoring convection in both current and future climate. Because of the simplicity, the simple model allows for physical interpretations to better understand how changes in the environmental profiles influence convection under global warming. Secondly, it emphasizes the crucial role of thermodynamic environmental fields (temperature and moisture) in determining mean convective activity state, highlighting the necessity for GCMs to simulate a better thermodynamic fields in future climate projection. Thirdly, it quantifies the effects of dynamical lifting and boundary layer moistening in triggering convection, which should be a source of uncertainty in current GCM projection. Lastly, it supports the dominant role of cold pool dynamics in controlling MCS genesis and its possible changes under the global warming, providing insights for developing model parameterization. This modeling framework can be elaborated and extended in several ways. For example, atmospheric gravity waves are important dynamics that communicate across columns producing organized convection (**???**). It is interesting to incorporate the effects of gravity waves into the model and investigate how it impacts the MCS genesis under the global warming. Besides, it is also important to further extend the model to 3-D so that it accounts for more realistic convection organization during the convective initiation and MCS genesis stages of the MCS life cycle. The model itself should be a useful tool for investigating the impact of global warming on MCS convection in both tropics and midlatitudes.

Acknowledgments. This research is supported by the U.S. Department of Energy Office of Science Biological and Environmental Research as part of the Regional and Global Model Analysis program area. PNNL is operated for the Department of Energy by Battelle Memorial Institute under contract DE-AC05-76RL01830.

Data availability statement. The ERA5 data can be downloaded from the Climate Data Store (CDS) website (`https://cds.climate.copernicus.eu/cdsapp#!/dataset/reanalysis-era5-pressure-levels?tab=overview`). The data from 37 CMIP5 models and all model output in this study are available on application to the corresponding author.